Computational modeling identifies multitargeted kinase inhibitors as effective therapies for metastatic, castration-resistant prostate cancer

Thomas Bello[a,b,1], Claudia Paindelli[c,d,e,1], Luis A. Diaz-Gomez[f], Anthony Melchiorri[f], Antonios G. Mikos[f], Peter S. Nelson[a], Eleonora Dondossola[c,d,2,3], and Taranjit S. Gujral[a,b,2,3]

[a]Human Biology Division, Fred Hutchinson Cancer Research Center, Seattle, WA 98109; [b]Department of Molecular and Cellular Biology, University of Washington, Seattle, WA 98195; [c]Department of Genitourinary Medical Oncology, The University of Texas MD Anderson Cancer Center, Houston, TX 77030; [d]David H. Koch Center for Applied Research of Genitourinary Cancers, The University of Texas MD Anderson Cancer Center, Houston, TX 77030; [e]Department of Cell Biology, Radboud Institute for Molecular Life Sciences, Radboud University Medical Center, 6525 GA Nijmegen, The Netherlands; and [f]Department of Bioengineering, Rice University, Houston, TX 77030

Edited by Arul M. Chinnaiyan, University of Michigan Medical School, Ann Arbor, MI, and approved August 18, 2021 (received for review February 25, 2021)

Castration-resistant prostate cancer (CRPC) is an advanced subtype of prostate cancer with limited therapeutic options. Here, we applied a systems-based modeling approach called kinome regularization (KiR) to identify multitargeted kinase inhibitors (KIs) that abrogate CRPC growth. Two predicted KIs, PP121 and SC-1, suppressed CRPC growth in two-dimensional in vitro experiments and in vivo subcutaneous xenografts. An ex vivo bone mimetic environment and in vivo tibia xenografts revealed resistance to these KIs in bone. Combining PP121 or SC-1 with docetaxel, standard-of-care chemotherapy for late-stage CRPC, significantly reduced tibia tumor growth in vivo, decreased growth factor signaling, and vastly extended overall survival, compared to either docetaxel monotherapy. These results highlight the utility of computational modeling in forming physiologically relevant predictions and provide evidence for the role of multitargeted KIs as chemosensitizers for late-stage, metastatic CRPC.

kinase | prostate cancer | computational modeling | combination therapy

According to the latest global cancer statistics (GLOBOCAN 2020), prostate cancer is the second-most common cancer in men, resulting in ∼1.4 million new cases and over 375,000 deaths in 2020 (1). Although the vast majority of patients diagnosed with the localized disease will respond well to treatment, metastatic, castration-resistant prostate cancer (mCRPC) remains a leading cause of cancer-related deaths in US males (2). Late-stage mCRPC exhibits poor responses to current therapeutic strategies and results in progressive disease relapse, pain, and other morbidities. This is especially true when the disease spreads to the bone, the most common site for distant growth (84% of metastatic sites) (2, 3). Current treatment options for mCRPC include drugs that target androgen receptor (AR) and androgen biosynthesis pathway, chemotherapy, immunotherapy, radiotherapy, and targeted therapy (PARP inhibitors). However, given the limited effectiveness of the existing treatments, additional strategies are urgently needed.

Recent studies suggest that up-regulation of compensatory, kinase-mediated signaling pathways plays an important role in mCRPC progression, in addition to the known roles of AR amplification, expression of AR splice variants, and stromal-mediated survival (4–6). Protein kinases play key roles in numerous biological processes of both normal and altered cells, including cancer cells (7), and represent a major drug target class. To date, 37 kinase inhibitors (KIs) have been approved by the US Food and Drug Administration (FDA), most for oncology-related indications (8). The ability to specifically target aberrant cellular signaling via kinase inhibition has proven to be a very effective cancer therapy, beginning with the FDA approval of imatinib (Gleevec) for the treatment of BCR-Abl–mutated, chronic myeloid leukemia (9). However, despite being developed as selective, multiple studies have demonstrated that most KIs, including ones approved for clinical use, display some level of target promiscuity (10, 11). While target promiscuity is generally considered undesirable, as it could lead to toxicity and side effects, the simultaneous inhibition of multiple, parallel signaling pathways or multiple nodes in a single pathway may provide improved efficacy and reduce the incidence of drug resistance. This led to the concept of "polypharmacology," and the growing awareness that polypharmacology is critical to the clinical effectiveness of KIs (12), especially in the context of polygenic and complex diseases, including mCRPC, which feature dysregulation in multiple kinase pathways. Additionally, the disappointing results from Phase III clinical trials of KIs for treatment of mCRPC (13) seem to support the idea that a polypharmacology-based strategy may be needed.

Here, to investigate the possibility of targeting kinase signaling for the treatment of mCRPC, we applied our established, unbiased approach called kinome regularization (KiR) (14). KiR is a method of target deconvolution that harnesses the polypharmacology of KIs

Significance

Metastatic, castration-resistant prostate cancer (mCRPC) is an advanced prostate cancer with limited therapeutic options and poor patient outcomes. To investigate whether multitargeted kinase inhibitors (KIs) represent an opportunity for mCRPC drug development, we applied machine learning–based functional screening and identified two KIs, PP121 and SC-1, which demonstrated strong suppression of CRPC growth in vitro and in vivo. Furthermore, we show the marked ability of these KIs to improve on standard-of-care chemotherapy in both tumor response and survival, suggesting that combining multitargeted KIs with chemotherapy represents a promising avenue for mCRPC treatment. Overall, our findings demonstrate the application of a multidisciplinary strategy that blends bench science with machine-learning approaches for rapidly identifying KIs that result in desired phenotypic effects.

Author contributions: T.B., E.D., and T.S.G. designed research; T.B., C.P., E.D., and T.S.G. performed research; T.B., C.P., L.A.D.-G., A.M., A.G.M., P.S.N., and T.S.G. contributed new reagents/analytic tools; T.B., C.P., P.S.N., E.D., and T.S.G. analyzed data; and T.B., C.P., P.S.N., E.D., and T.S.G. wrote the paper.

The authors declare no competing interest.

This article is a PNAS Direct Submission.

This open access article is distributed under Creative Commons Attribution-NonCommercial-NoDerivatives License 4.0 (CC BY-NC-ND).

[1]T.B. and C.P. contributed equally to this work.

[2]E.D. and T.S.G. contributed equally to this work.

[3]To whom correspondence may be addressed. Email: tgujral@fredhutch.org or EDondossola@mdanderson.org.

This article contains supporting information online at https://www.pnas.org/lookup/suppl/doi:10.1073/pnas.2103623118/-/DCSupplemental.

Published September 30, 2021.

Downloaded by guest on January 7, 2022

to identify critical kinases involved in a specific cellular function. KiR relies on a large-scale dataset that quantitatively characterizes the target inhibition profiles of over 400 KIs. We reduced and captured this complexity in a computationally chosen subset of ∼32 broadly specific KIs to test on the desired model system (14). Using elastic net regression modeling, KiR identifies the kinases whose activities most likely contribute to a measured phenotype (e.g., cell growth) (15). KiR currently covers 298 human kinases and has been validated in a panel of liver, lung, and breast cancer cell lines (16) and malaria (17). Using KiR, we identified two multitarget small-molecule inhibitors, PP121 and SC-1, that effectively inhibited CRPC growth across many model systems. In vitro assays demonstrated that both PP121 and SC-1 significantly reduced cellular confluence across different CRPC cell lines and abrogated phosphorylation on multiple growth signaling proteins, exhibiting a cytostatic effect. Both compounds also showed the significant growth suppression of in vivo subcutaneous xenograft CRPC tumors. Finally, orthotopic xenografts in mouse tibiae, a model of bone metastasis, showed that, while neither KI inhibited the growth of the tumors on their own, both PP121 and SC-1 dramatically improved survival and decreased tumor sizes when administered in combination with docetaxel, a standard-of-care chemotherapeutic for CRPC. These results demonstrate the marked ability of these KIs to improve on docetaxel in both tumor response and survival and demonstrate that combining multitargeted KIs with chemotherapy represents a promising avenue for mCRPC treatment.

Results

Kinase Inhibitor Functional Screen Leads to Predictive Models of CRPC Growth. To begin predicting suitable KI candidates for CRPC treatment, we applied our KiR pipeline, as described (14). Briefly, we began with a previously published dataset that quantifies the effect of over 400 KIs on 298 recombinant human protein kinases (∼56% of the human kinome; Dataset S1) using a radioisotope-labeled ATP assay, a well-established standard for measuring catalytic activity (11, 18). These pairwise inhibition profiles were represented as the percent of residual kinase activity in the presence of the KI (compared to untreated controls) (11). The unsupervised hierarchical clustering of the full inhibition profiles divided the >400 KIs into distinct groups, from which we formed a subset of ∼30 KIs by picking one from each group so as to maximize the overall coverage of the profiled human kinome (*SI Appendix*, Fig. S1*A*). We supplemented this screening set with an additional ∼20 KIs in each cell line, as needed, to ensure a sufficient range of observed responses. This increased number of observations also allowed us to later withhold observations from the models to validate the models' predictions.

We performed our functional KI screen in four CRPC cell lines: PC3, C4-2B, DU145, and 22Rv1 (Fig. 1*A*). These lines have been used extensively in prostate cancer research and account for a variety of biological phenotypes, including AR activity and the tissue of origin (C4-2B and 22Rv1 exhibit AR activity, while PC3 and DU145 do not; PC3 and C4-2B are derived from bone metastases, DU145 from brain metastasis, and 22Rv1 from a primary tumor) (19). In our assay, each line was seeded in 96-well cell culture plates and treated with ∼50 KIs at seven doses (plus untreated control), ranging from 10 to 0.01 μM, in triplicate for each dose. This dose range captures the full response range for nearly all inhibitors, with the lowest dose rarely differing from the controls for any inhibitor. The highest dose displays a near-maximal potency for most drugs without exhibiting significant, nonspecific effects (such as DMSO vehicle toxicity). Images of each well were taken every 2 h using the IncuCyte ZOOM imaging system for 48 to 96 h (20). Cellular confluence was quantified using the IncuCyte ZOOM software to identify a cell mask and divide the area occupied by cells by the total image area, as described previously (Fig. 1*B*) (21). To account for varying growth rates between cells, we calculated our end point response as the net change in confluence (Δconfluence) between the first image posttreatment and the time point when the control samples within the same plate reached 75% confluence (*SI Appendix*, Fig. S1*B*). The Δconfluence was normalized to have a pseudomaximum of 1 (or 100%) for untreated controls, with most data points falling in the range from 0 to 1 (inhibitors that caused a decrease in confluence from the first time point resulted in a negative Δconfluence). We generated dose–response data for each cell line–inhibitor combination, fit the data with a three-parameter logistic equation, and interpolated the resulting curve at the doses for which the compounds were profiled (generally 500 nM) (Fig. 1 *C* and *D*) (6). We defined an "effective" inhibitor as one that reduced Δconfluence by at least 30% compared to untreated controls (i.e., final Δconfluence was <70% of control; see justification in *Model-Predicted Compounds PP121 and SC-1 Inhibit CRPC Growth and Signaling In Vitro*). At the interpolated doses, 13 KIs were effective in PC3 cells, 14 in 22Rv1 cells, and 12 in each C4-2B and DU145 cells (Dataset S2). These interpolated responses served as the basis for our predictive KiR models.

To generate the KiR models, we partitioned the observed KI responses into empirically determined training and validation sets for each cell line, ensuring a sufficient number of both effective and ineffective inhibitors in each set (Dataset S2). The interpolated Δconfluence for each training set KI was used as the response variable for elastic net–regularized multiple linear regression (14, 20, 22, 23). The explanatory variables in this regression were the residual activities of the 298 human kinases in the presence of these selected inhibitors. The penalty imposed by elastic net regularization restricted the number of variables included in the model (i.e., number of kinases with nonzero coefficients), with the optimal regularization penalty (λ) selected via leave-one-out cross-validation (LOOCV) (*SI Appendix*, Fig. S1*C*). Root mean–squared error (RMSE) values for the models' predictions compared to the training set observations ranged from 0.00919 for C4-2B cells to 0.0896 for 22Rv1 cells, giving us confidence that the models accurately represented the training set observations (*SI Appendix*, Table S1). Because the explanatory variables were the previously measured inhibition profiles of the KIs, we used the preliminary KiR models' coefficients, calculated from the initial screening set, to predict the Δconfluence response for all >400 profiled KIs, including the compounds in the validation sets and hundreds of untested compounds (*SI Appendix*, Fig. S1*D* and Dataset S2). Comparing these predictions to the naïve validation set observations, we calculated validation RMSEs that ranged from 0.1598 for PC3 to 0.2763 for C4-2B (*SI Appendix*, Table S1). As expected, the validation set errors are higher than the training set errors, but they nevertheless gave us confidence that these models captured sufficient information in the training sets to accurately predict the responses in the validation sets (and all of the untested KIs). The final validated KiR models resulted in measured or predicted cellular responses to over 400 KIs across the four CRPC cell lines (Fig. 1 *E*–*H* and Dataset S2).

Model-Predicted Compounds PP121 and SC-1 Inhibit CRPC Growth and Signaling In Vitro. While we identified several cell type–specific inhibitors, we were motivated to identify compounds that were effective in all four cell lines. Thus, we defined an effective compound as one that had a measured or predicted (if measured was unavailable) Δconfluence at least 30% less than control at the interpolated dose. This cutoff maximized the number of compounds correctly predicted by the KiR models to be effective (i.e., above the cutoff) or ineffective (below the cutoff) when compared to experimental observations, while still maintaining a meaningful threshold (Dataset S3). A total of eight compounds met this criterion (Fig. 2*A*). Pearson correlations of these compounds' target profiles showed that they generally fell into four

Downloaded by guest on January 7, 2022

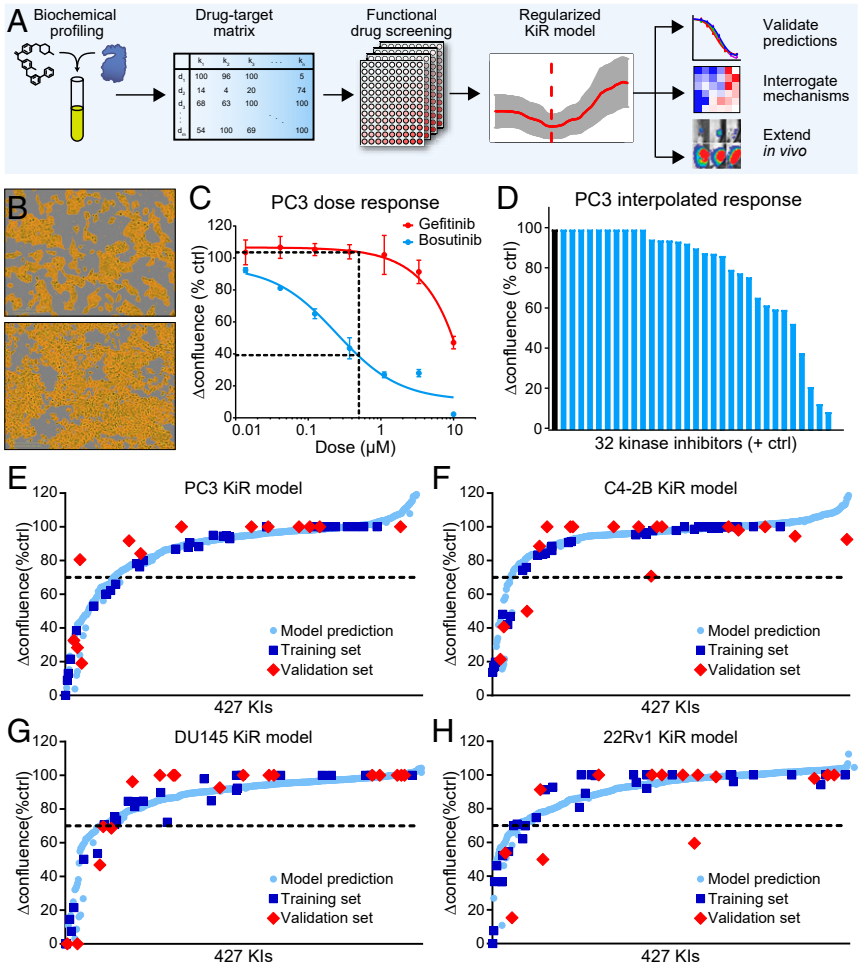


Fig. 1. Constructing predictive KiR models from an in vitro KI screen. (*A*) Schematic of KiR workflow. Previous biochemical profiling of KIs resulted in a quantitative drug–target matrix. From this, an optimal set of ~32 KIs are used for a small-scale drug screen. The results enable the generation of a regularized, cross-validated model that predicts the responses to over 400 KIs. (*B*) Representative images of PC3 cells after 52 h of treatment with bosutinib at 3.33 (*Top*) or 0.01 μM (*Bottom*). Cell confluence mask (shown in orange) was drawn and quantified via IncuCyte ZOOM. *Top* image was quantified at 45.6% confluent and bottom image at 72.6% confluent. (*C*) Representative dose–response curves of PC3 treated with bosutinib or gefitinib. Curves are fitted with a three-parameter logistic equation, and responses were interpolated at 500 nM. Mean ± SEM and $n = 3$ wells/dose. (*D*) Interpolated responses of PC3 cells to the tested inhibitors. (*E–H*) KiR model plots for four CRPC cell lines, showing the response of each cell line to 427 KIs (different doses of the same compound are profiled separately and thus treated as separate compounds for this purpose). Light blue circles represent KiR model predictions, dark blue squares represent experimentally measured values used to train the model, and red diamonds represent experimentally measured values used for validation and are not included in the final model construction. The dotted line indicates the threshold (<70% of control) for an inhibitor to be considered effective. ctrl, control.

clusters (Fig. 2*B*). The first cluster included three broad-spectrum inhibitors (CDK 1/2 inhibitor III, staurosporine, and PDK/AKT/FLT dual-pathway inhibitor) that are known to have pleiotropic effects and inhibit cellular growth in most model systems. Using our previously published KI selection portal, KInhibition, we quantified the selectivity of these compounds toward various receptor tyrosine kinases (RTKs) and signaling nodes (growth factor receptors, Src family kinases, Abl, etc.) (Dataset S4). For each KI, we calculated the KInhibition Selectivity Score (KISS) as a measure of KI selectivity (KISS of 100 represents full on-target activity, while KISS of −100 represents the opposite) (24). Out of the KIs we identified here, CDK 1/2 inhibitor III, staurosporine, and PDK/AKT/FLT dual-pathway inhibitor had KISS values of −24.49, −12.65, and −22.47, respectively, reinforcing their promiscuity and were thus excluded from further analysis. Dasatinib (KISS of −11.07) has shown efficacy against CRPC in preclinical settings but failed to increase overall survival in the Phase III clinical trial, so we chose not to pursue this compound and a very similar compound (NCGC00348110), despite their notable in vitro results (25). Of the remaining two clusters, PP121 (KISS of 15.49) seemed the most unique, and SC-1 (KISS of 23.45) showed greater growth suppression than the molecule it clustered with (PD 166285 dihydrochloride, KISS of 4.10). Notably, treatment with PP121 and SC-1 potently inhibited the growth of all four CRPC cells lines tested: two additional AR-positive CRPC cells lines, including LNCaP42D and LuCaP35CR (Fig. 2 *C–D* and *SI Appendix*, Fig. S3), and the viability of organotypic tumor slices (26) prepared from two independent, patient-derived xenografts (PDX) CRPC models (*SI Appendix*, Fig. S4). Since both PP121 and SC-1 showed potent, dose-dependent growth suppression across all cell lines tested (Fig. 2 *C* and *D* and *SI Appendix*, Fig. S2), we chose to proceed with these compounds for further validation.

PP121 was developed as a dual inhibitor of tyrosine kinases and phosphoinositide 3-kinases (PI3Ks) (27) and was shown to inhibit PI3Ks, RTKs, and Src family kinases. PP121 was reported to block the proliferation of glioblastoma, thyroid, and other tumor cells and inhibit multiple, oncogenic or mutated kinases (28). SC-1, also known as pluripotin, inhibits Erk1 (MAPK3) and RasGAP (RASA1) and blocks differentiation pathways in

Downloaded by guest on January 7, 2022

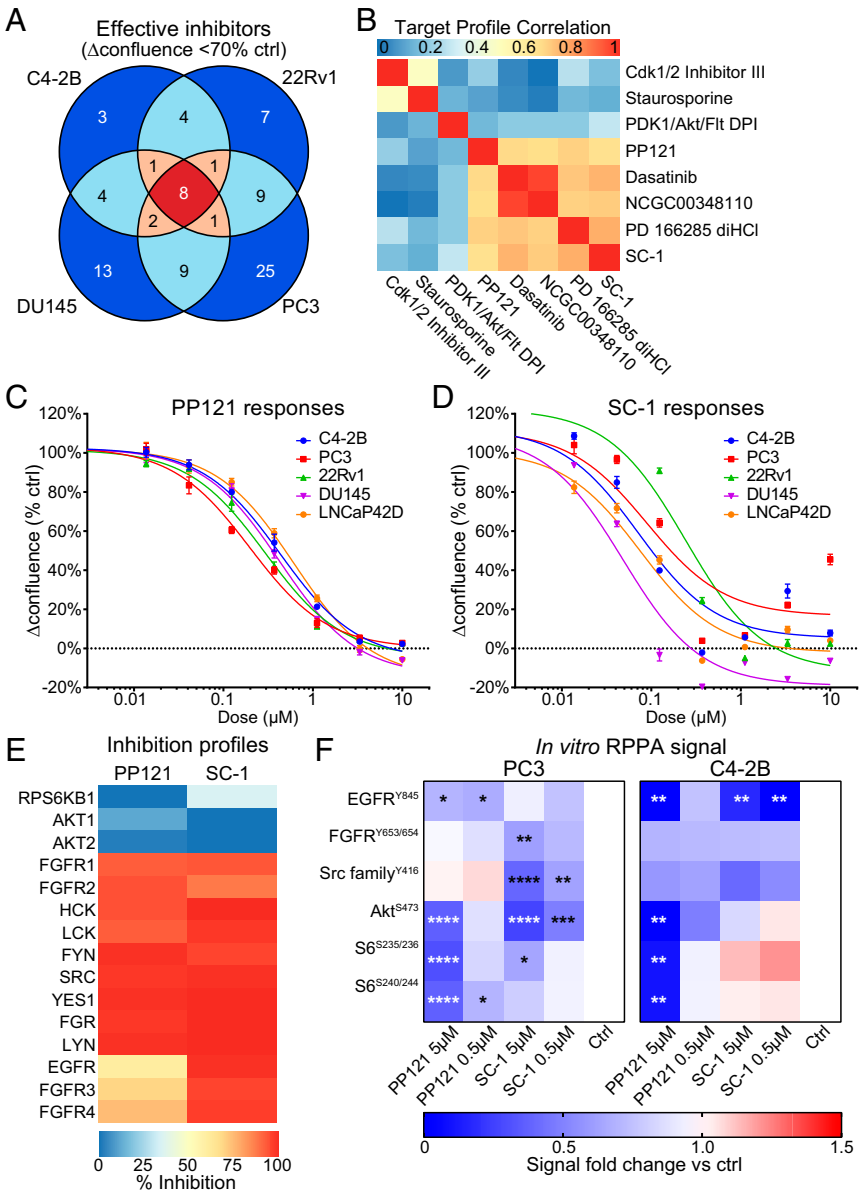


Fig. 2. PP121 and SC-1 effectively target CRPC cells in vitro. (*A*) Euler diagram of the effective inhibitors in all four cell lines. Eight inhibitors reduced the change in confluence to <70% of untreated control in all four cell lines. Two inhibitors effective only in 22Rv1 and DU145 cell lines were unable to be represented here. (*B*) Pearson correlation heatmap of the inhibition profiles of the eight effective inhibitors from *A*. (*C* and *D*) Cell line dose–responses to two of the most effective inhibitors, PP121 (*C*) and SC-1 (*D*). Mean ± SEM and $n = 3$ wells/dose. (*E*) Biochemically assayed inhibition profiles of PP121 and SC-1 toward receptors EGFR and FGFR and downstream signaling molecules Src family kinases, Akt and S6 kinase. (*F*) Heatmaps of RPPA phosphorylation signals when PC3 and C4-2B cells are treated with PP121 or SC-1 in vitro. Signal is normalized to β-actin and presented relative to DMSO control. *$P < 0.05$, **$P < 0.01$, ***$P < 0.001$, ****$P < 0.0001$, and two-way ANOVA with Holm–Sidak multiple comparisons test.

embryonic stem cells, although its kinase inhibition profile demonstrates broader activity against many tyrosine kinases (11, 29). To further characterize the molecular effects of PP121 and SC-1 on prostate cancer cells in vitro, we measured changes in the phosphorylation of several signaling proteins in response to low- or high-dose, short-term treatment with PP121 or SC1 using reverse-phase protein array (RPPA), a miniaturized dot blot technique that allows the screening of multiple signaling proteins and pathways across many samples (30). PC3 and C4-2B cells were treated in vitro with 5 or 0.5 μM of PP121 or SC-1 (plus DMSO control) for 1 h. RPPA results were quantified as the fluorescent signal intensity from each spot, normalized to the β-actin signal intensity from the same spot, and presented relative to DMSO controls. We assayed phosphorylation changes in a subset of proteins involved in growth signaling, including EGFR, FGFR, Src family kinases, Akt, and small ribosomal protein S6. These proteins have been reported to play key roles in the growth and progression of late-stage prostate cancer (4, 31–33). The biochemical inhibition profiles of PP121 and SC-1 suggest that these compounds effectively inhibit EGFR, FGFR, and Src family kinase signaling (Fig. 2*E*). The results showed a strong trend toward decreasing growth factor signaling in both cell lines, with PC3 tumors exhibiting more significant responses (Fig. 2*F*). The higher dose (5 μM) of PP121 significantly reduced EGFR, Akt, and S6 phosphorylation in both cell lines (PC3 cells: $P < 0.05$, $P < 0.0001$, and $P < 0.0001$, respectively; C4-2B cells: $P < 0.01$ for all signals; Fig. 2*F*). SC-1 abrogated Src family kinase and Akt phosphorylation at both doses in PC3 cells (5 μM, $P < 0.0001$ for both signals; 0.5 μM, $P < 0.01$ and $P < 0.001$, respectively), while only significantly

Downloaded by guest on January 7, 2022

affecting EGFR phosphorylation in C4-2B cells ($P < 0.01$, both doses). In addition, we also explored whether PP121 or SC-1 could affect AR signaling. The treatment of C4-2B cells with biologically active doses of either PP121 (1 μM) or SC-1 (1 μM) induced no or modest changes in the expression of AR-targeted genes (4), with few exceptions (*SI Appendix*, Fig. S5*A*). In comparison, treatment with enzalutamide (1 μM) significantly decreased the expression of all AR-targeted genes, suggesting that the mechanism of action of both PP121 and SC-1 is likely complementary to AR-targeting agents, thus representing a potential alternative strategy in case of resistance emergence. Overall, the inhibition of growth factor signaling in both PC3 and C4-2B upon PP121 and SC-1 treatment provides a preliminary molecular basis for how these compounds inhibit CRPC growth, consistent with previous reports of these proteins' role in driving late-stage prostate cancer (4, 31–33).

PP121 and SC-1 Inhibit CRPC Growth In Vivo. To investigate PP121 and SC-1 efficacy in vivo, we implanted mice subcutaneously with luciferase-positive PC3 or C4-2B cells (Fig. 3*A*). Around 10 d postimplantation, mice were treated with PP121 (150 mg/kg) or SC-1 (80 mg/kg) 5 times/wk, for 2 wk, by oral gavage, and tumor growth was monitored over time (Fig. 3*B*). C4-2B tumor growth was measured by macroscopic bioluminescence. Since PC3 cells grew at a fast rate, generating palpable tumors by day 10 already (leading to a saturated bioluminescent signal), we measured tumor growth with the help of a caliper. Our data show that the administration of either KI as a single agent showed a fourfold reduction in both PC3 and C4-2B tumor growth (SC-1 treated PC3 tumors: $P < 0.05$; all other treatments: $P < 0.01$; Fig. 3*C*). Weighing the tumor mass at the end point showed an average of over a 50% decrease in final PC3 tumor weight with either KI treatment ($P < 0.05$) and an average of nearly 80% reduction in final C4-2B tumors weight ($P < 0.001$; Fig. 3 *D* and *E*). Consistently, the molecular analyses of the PP121- or SC-1–treated tumors revealed a reduction in the phosphorylation of multiple growth factors signaling proteins, including the phosphorylation of Src family kinases, EGFR, and FAK compared with vehicle-treated controls (*SI Appendix*, Fig. S5*B*). Notably, both compounds were well tolerated by mice, with no significant overall weight loss, as monitored at the end point (Fig. 3*F*). Other parameters evaluated during the experiments included hydration, breathing difficulties, aberrant behavior and movements, and abdominal cavity swelling, with no evidence of any of these complications. Therefore, both PP121 and SC-1 exhibit beneficial therapeutic activity in vivo.

KIs Monotherapy Efficacy Is Reduced in Bone Metastasis Models of CRPC. Bone metastasis is the most frequent and lethal complication of CPRC progression (3). To assess KI efficacy in bone lesions, mice implanted in the tibia with luciferase-positive PC3 or C4-2B cells (Fig. 4*A*) were treated with PP121 (150 mg/kg) or SC-1 (80 mg/kg; Fig. 4*B*). As previously shown, such doses were well tolerated by mice, with no significant weight loss over time (*SI Appendix*, Fig. S6 *A* and *B*) and no evidence of other complications (e.g., reduced hydration, difficulties in breathing, aberrant behavior and movements, and abdominal cavity swelling). Tumor growth, monitored by macroscopic bioluminescence analysis, showed no significant, KI-mediated tumor reduction for either cell line (Fig. 4*C*). The failure of therapeutic agents administered as monotherapy in bone is not surprising and is supported by several documented mechanisms, including osteoblast-mediated resistance (34, 35). Accordingly, we compared the therapeutic activity of PP121 and SC-1 in two-dimensional (2D) monoculture or in an organotypic bone mimetic environment (BME) of metastasis that proved to mimic pathophysiological aspects of the metastatic bone niche, including in vivo–like mechanisms of response and resistance to therapy (27). Briefly, the BME consists of round polycaprolactone scaffolds shaped to fit a 96-well plate (6-mm diameter

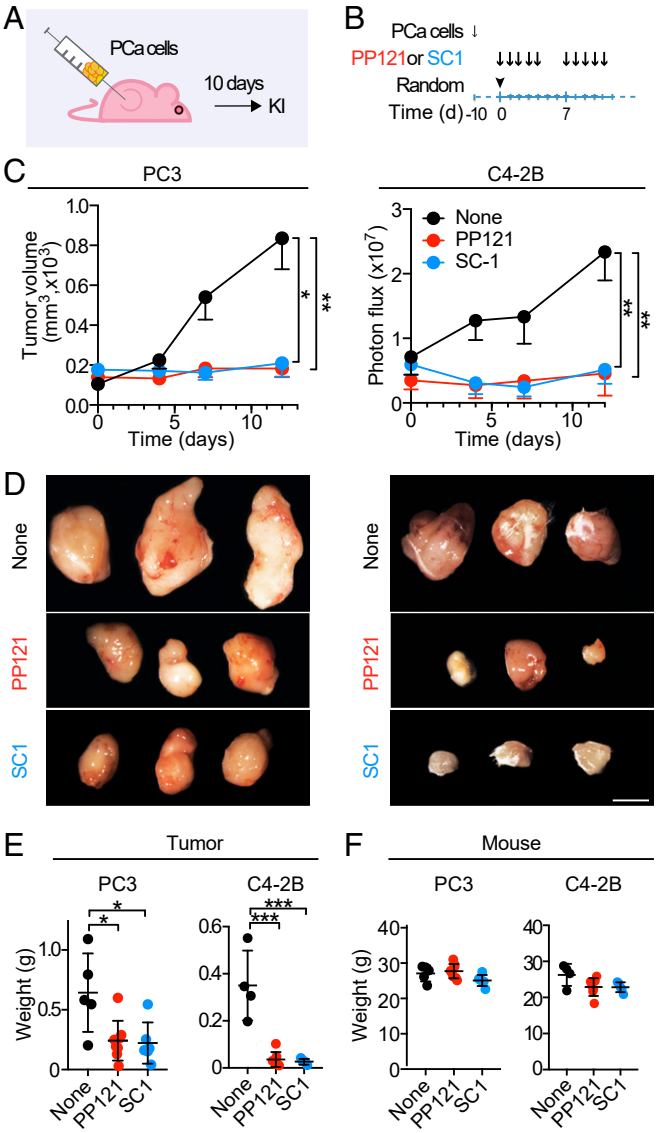


Fig. 3. PP121 and SC-1 significantly reduced tumor growth in vivo. (*A*) Schematic representation of the experiment; mice were implanted with prostate cancer cells (PCa) subcutaneously; and, after 10 d, mice were treated with KI, and the response was assessed longitudinally using a caliper (PC3) or monitoring the bioluminescent signal. (*B*) Timeline of in vivo KIs treatments. At day 10, after tumor implantation (5×10^6 PC3 cells/mouse and 6×10^6 C4-2B cells/mouse), mice were randomized and treated with 150 mg/kg PP121 or 80 mg/kg SC-1. (*C*) KI treatment response of PC3 and C4-2B subcutaneous tumors. Tumor growth is shown, mean ± SD, and $n = 4$ to 8 tumors per group. (*D*) Pictures of representative tumors are shown. (*E* and *F*) Tumor (*E*) and mouse (*F*) weight for both KI treatments were quantified at the end point. $^*P < 0.05$, $^{**}P < 0.01$, $^{***}P < 0.001$, and one-way ANOVA followed by Tukey's honestly significant difference post hoc test.

and 0.2-mm thickness), colonized by human mesenchymal stem cells (hMSCs), differentiated toward the osteoblastic lineage for 4 wk in osteoinductive medium (Fig. 4*D*). The spheroids of PC3 cells that mimic small avascular lesions were cultivated on the BME for 3 d, then PP121 or SC-1 at a concentration of 0.5 or 5 μM were added to the culture, and the outcome recorded by live-cell microscopy over time, followed by the quantification of fluorescence intensity. While PP121 significantly reduced tumor growth in 2D culture, even at 0.1 μM ($P < 0.001$), this KI showed no effect at 0.5 μM in the BME and only exhibited growth suppression at 5 μM

Downloaded by guest on January 7, 2022

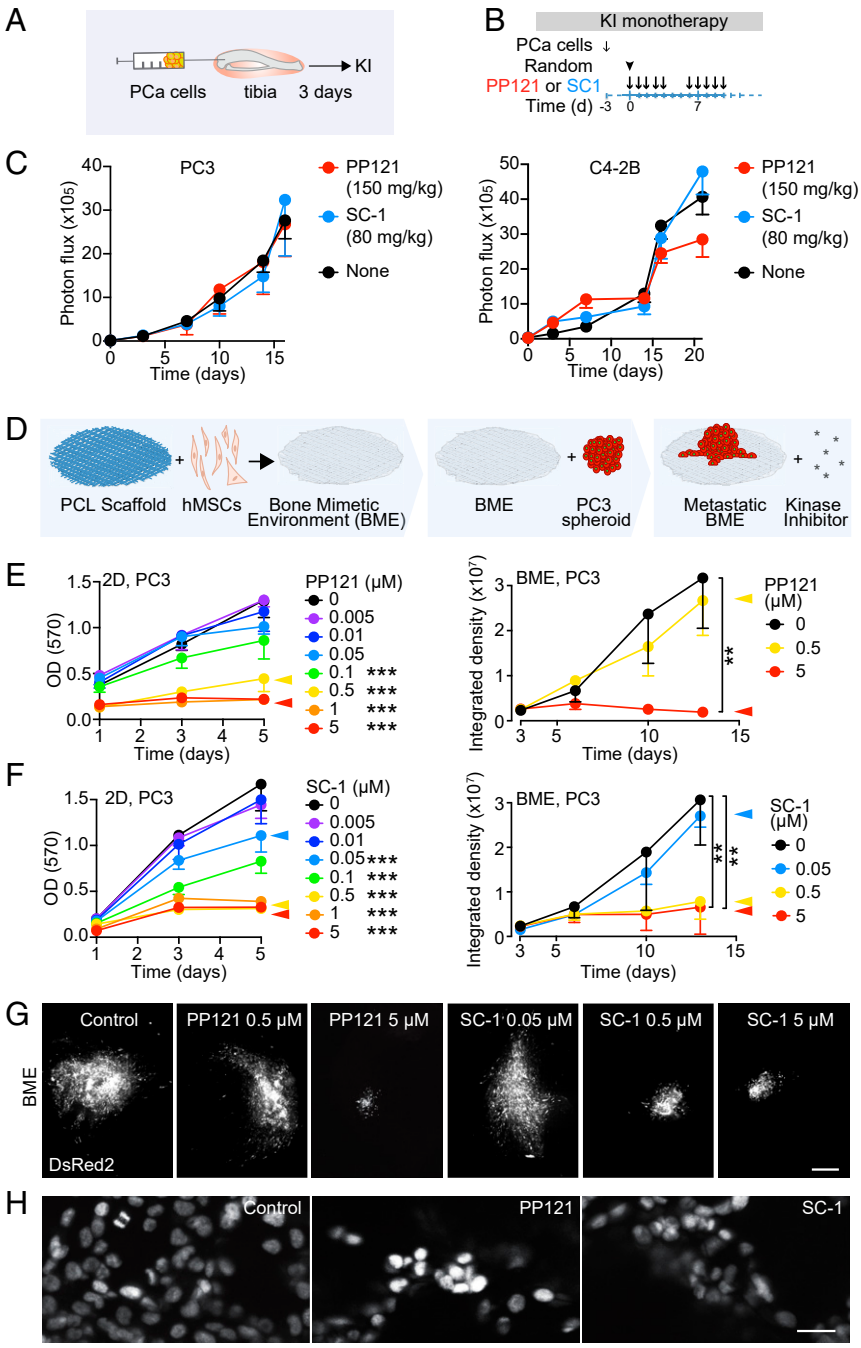


Fig. 4. Response to KI treatment by prostate cancer cells (PCa) cells in bone, in vivo, and in vitro. (*A*) Schematic representation of in vivo treatment schedule. PCa cells were implanted by intratibial injection, and the response to KI treatment was assessed longitudinally monitoring the bioluminescence signal. (*B*) Timeline of in vivo KIs treatment. At day 3, after tumor implantation (2.5×10^5 PC3 cells/ tibia and 5×10^5 C4-2B cells/ tibia), mice were randomized and treated with 150 mg/kg PP121 or 80 mg/kg SC-1. (*C*) KI treatment response of PC3 and C4-2B cells in bone. Tumor growth is shown, mean ± SD, and $n = 8$ to 10 tibiae per group. (*D*) Schematic representation of the BME development and application to assess the response of PCa cells to KIs in vitro. Native polycaprolactone (PCL) scaffolds were functionalized with hMSCs, differentiated to osteoblasts in osteogenic medium to generate a mature BME. Spheroids made with dual-color PC3 cells (expressing nuclear H2B/eGFP and cytoplasmic DsRed2) and were seeded on the BME to mimic avascular cancer lesions. The metastatic BME is used to assess the response to targeted KIs. (*E* and *F*) PC3 cell growth in 2D (*Left*) or in the BME (*Right*) in the presence of different doses of KIs was monitored by crystal violet staining or integrated density (fluorescence) analysis, respectively, for both PP121 (*E*) and SC-1 (*F*). Mean ± SD and $n = 4$ well/condition or $n = 5$ BMEs/condition. $^{**}P < 0.01$, $^{***}P < 0.001$, and one-way ANOVA followed by Tukey's honestly significant difference post hoc test. (*G*) Epifluorescence microscope overview images of spheroids made with dual-color PC3 8 d after treatment. DsRed2 is shown. (Scale Bar, 300 μm.) (*H*) Representative detailed images. (Scale Bar, 20 μm.)

($P < 0.01$; Fig. 4 *E–G*). Similarly, SC-1 significantly decreased PC3 cell growth at 0.05 μM in 2D ($P < 0.001$) but lost efficacy at the same dose in the BME (Fig. 4 *E–G*). Spheroids treated with PP121 and SC-1 did not exhibit increased cell death based on fluorescent intensity, suggesting that these agents exert a cytostatic rather than a cytotoxic effect (Fig. 4 *G* and *H*). To further clarify the cell-autonomous effect of PP121 and SC-1 on cell death, we performed a dose–response study testing KI concentrations from 5 to

Downloaded by guest on January 7, 2022

0.005 μM on H2B/eGFP-positive PC3 cells in 2D, tracking the status of the nucleus (percentage of mitosis or apoptosis on total cell number; *SI Appendix*, Fig. S7). The treatment with both inhibitors significantly reduced the percentage of cells undergoing mitosis for doses up to 0.05 μM for SC-1 ($P < 0.05$) and 0.5 μM for PP121 ($P < 0.001$), as captured by fluorescence microscopy, while the percentage of apoptotic cells was not significantly affected, confirming a cytostatic activity (*SI Appendix*, Fig. S7). These results suggest that KI monotherapy, effective in mouse subcutaneous tumors, displays reduced efficacy in bone lesions.

KIs Increase the Efficacy of Docetaxel on In Vivo Bone Metastasis Model of CRPC. The combination of kinase inhibition with chemotherapy has shown increased efficacy in many different tumor types (36, 37). In pursuit of an improved outcome for mCRPC, we combined PP121 or SC-1 with docetaxel, a chemotherapeutic agent used as a standard of care in mCRPC, and tested the efficacy of this combination in vitro and in vivo. We combined 100 ng/mL docetaxel with 0.05 or 0.005 μM PP121 or SC-1, two doses that showed modest or no effects in previous experiments (Fig. 4 *E* and *F*). In combination with docetaxel, both doses for both KIs significantly increased the number of apoptotic cells compared to docetaxel alone (0.005 μM PP121: $P < 0.01$; all other treatments: $P < 0.001$; Fig. 5*A*), suggesting potential synergistic effects at low doses of KIs. We next set up in vivo combination studies. Initially, we performed a tumor-specific dose–response experiment to identify a dose of docetaxel that induces partial tumor regression and selected 15 mg/kg for PC3 and 7.5 mg/kg for C4-2B (*SI Appendix*, Fig. S8). Mice were implanted with prostate cancer cells in the tibiae and treated with PP121 or SC-1, as reported in *KIs Monotherapy Efficacy Is Reduced in Bone Metastasis Models of CRPC*, and docetaxel administration occurred 2 d after starting the treatment with the KIs (Fig. 5*B*). PC3 tumor growth was significantly affected by applying PP121 + docetaxel and SC-1 + docetaxel, showing a sixfold decrease compared to docetaxel alone ($P < 0.05$; Fig. 5*C*). C4-2B tumor growth was significantly affected by SC-1 + docetaxel ($P < 0.05$) but not by PP121 + docetaxel (Fig. 5*C*). No significant loss of weight was identified in any of the treated mice (*SI Appendix*, Fig. S6*A*). Besides decreasing tumor growth, both KIs significantly prolonged the overall survival in mice implanted with PC3 cells, with tumor-free mice up to 120 d ($P < 0.01$, Fig. 5*D*). SC-1 + docetaxel treatment prolonged survival in mice implanted with C4-2B tumors to a lesser extent ($P < 0.05$), while PP121 + docetaxel treatment did not significantly affect the overall survival (Fig. 5*D*). These results suggest a possible synergistic effect between docetaxel and multitargeted KIs against the bone metastasis of CRPC.

To confirm the increased sensitivity of cancer cells to the combination therapy in bone, we performed short-term in vivo xenograft experiments and subjected the resulting tumors to RPPA to monitor the molecular signaling landscape. We specifically focused on PC3 tumors, as they demonstrated the strongest phenotypic response to the therapies tested. Tumors were implanted in mouse tibiae, allowed to grow for 3 d, treated for 3 d with various combinations of KI monotherapy and docetaxel, then harvested, lysed, and subjected to RPPA (Fig. 5*E*). We used previously validated antibodies to assess the activation state of a small subset of proteins implicated in prostate cancer progression (EGFR, FGFR, Src family kinases, Akt, and S6). As expected, based on our single-agent results described in *KIs Monotherapy Efficacy Is Reduced in Bone Metastasis Models of CRPC* (Fig. 4*C*), none of the single-agent treatments (docetaxel, PP121, or SC-1) had any significant effect on the phosphosites we tested (Fig. 5 *F*, *Left heatmap*). In contrast, both combination therapies displayed striking changes in signaling. PP121 + docetaxel significantly decreased phosphorylated $S6^{S235/236}$ ($P < 0.001$) and $S6^{S240/244}$ ($P < 0.01$) levels compared to docetaxel-only treated tumors (Fig. 5 *F*, *Right heatmap*). SC-1 + docetaxel significantly decreased phosphorylated $EGFR^{Y1173}$ ($P < 0.0001$), $FGFR^{Y653/654}$ ($P < 0.01$), Src^{Y416} ($P < 0.01$), Akt^{S473} ($P < 0.05$), $S6^{S235/236}$ ($P < 0.0001$), and $S6^{S240/241}$ ($P < 0.0001$) compared to docetaxel-only treated tumors (Fig. 5 *F*, *Right heatmap*). This is concordant with both the in vitro (Fig. 4 *E* and *F*) and in vivo (Fig. 5*C*) phenotypic data. Taken together, these results demonstrate that combining docetaxel with multitargeted KIs, such as PP121 and SC-1, can improve both the phenotypic and molecular responses of prostate cancer in vivo compared to docetaxel alone.

Discussion

In this study, we applied a systems-based approach (KiR) that leverages the polypharmacology of KIs to identify agents with potential activity against mCRPC, a recalcitrant cancer that currently lacks effective treatment options. By mathematically coupling the results of the functional screen performed with a limited and highly curated set of KIs to the biochemical profiles of the KIs, we were able to significantly improve the scope, relevance, and predictive power of even this small-scale in vitro study. This approach identified PP121 and SC-1 as promising hits for further characterization in more complex model systems. Overall, PP121 and SC-1 monotherapy significantly abrogated the growth of both PC3 and C4-2B subcutaneous tumors, and both KIs were effective in the bone metastasis models of CRPC when combined with a chemotherapy agent docetaxel, despite lacking monotherapy activity in these systems. This disparity suggests that the bone microenvironment exerts a protective effect against KI therapy. Indeed, bone is a well-known site for conferring resistance to chemo- and molecular therapy in metastatic cancer via the release of soluble factors or through contact with stromal cells, including osteoblasts (34, 35). Our 3D BME system partly reproduced this effect, requiring significantly higher doses of PP121 and SC-1 to achieve the same growth suppression as in 2D monoculture. We overcame this resistance by combining PP121 or SC-1 with the chemotherapeutic docetaxel, which given these limitations of the monotherapy strategy, it was gratifying to see that the combination of docetaxel with PP121 or SC-1 synergized to abrogate CRPC tumor growth, extended lifespans, and suppressed growth factor signaling in tibia tumors in vivo.

Recently, second-generation antiandrogen therapies have been approved for use in men with metastatic, castrate-sensitive prostate cancer, based on the positive outcome of Phase III studies (38, 39), and their use has shifted from the castrate-resistant to castrate-sensitive setting. While data on the optimal sequencing of treatment regimens are lacking, men who develop metastatic CRPC after initial treatment with second-generation antiandrogen therapies in the castrate-sensitive disease state are frequently prescribed docetaxel, given high cross-resistance between different second-generation antiandrogen therapies (40). Interestingly, our KIs do not significantly affect AR downstream signaling (*SI Appendix*, Fig. S5*A*), suggesting their use as a potential alternative strategy in case of resistance emergence. Considering these observations, we posit combination therapy involving KIs and docetaxel as a clinically relevant, therapeutic opportunity for the treatment of metastatic CRPC.

Although our results are promising and offer an opportunity for the future exploration of both the use of KiR as a method for rapidly identifying KIs that result in desired phenotypic effects and the use of PP121 and SC-1 as leads for CRPC drug development, we acknowledge some outstanding challenges related to kinase-targeted therapy for prostate cancer. For example, a KI is yet to be approved for the treatment of prostate cancer, as monotherapy or in combination with chemotherapy. In a Phase III trial concluded in 2013, the combination of the KI dasatinib with docetaxel failed to improve overall survival, compared to docetaxel alone (25). This highlights the need for more extensive preclinical assessment, data-informed dosing schedules, and specific biomarkers to stratify patient populations and identify

Downloaded by guest on January 7, 2022

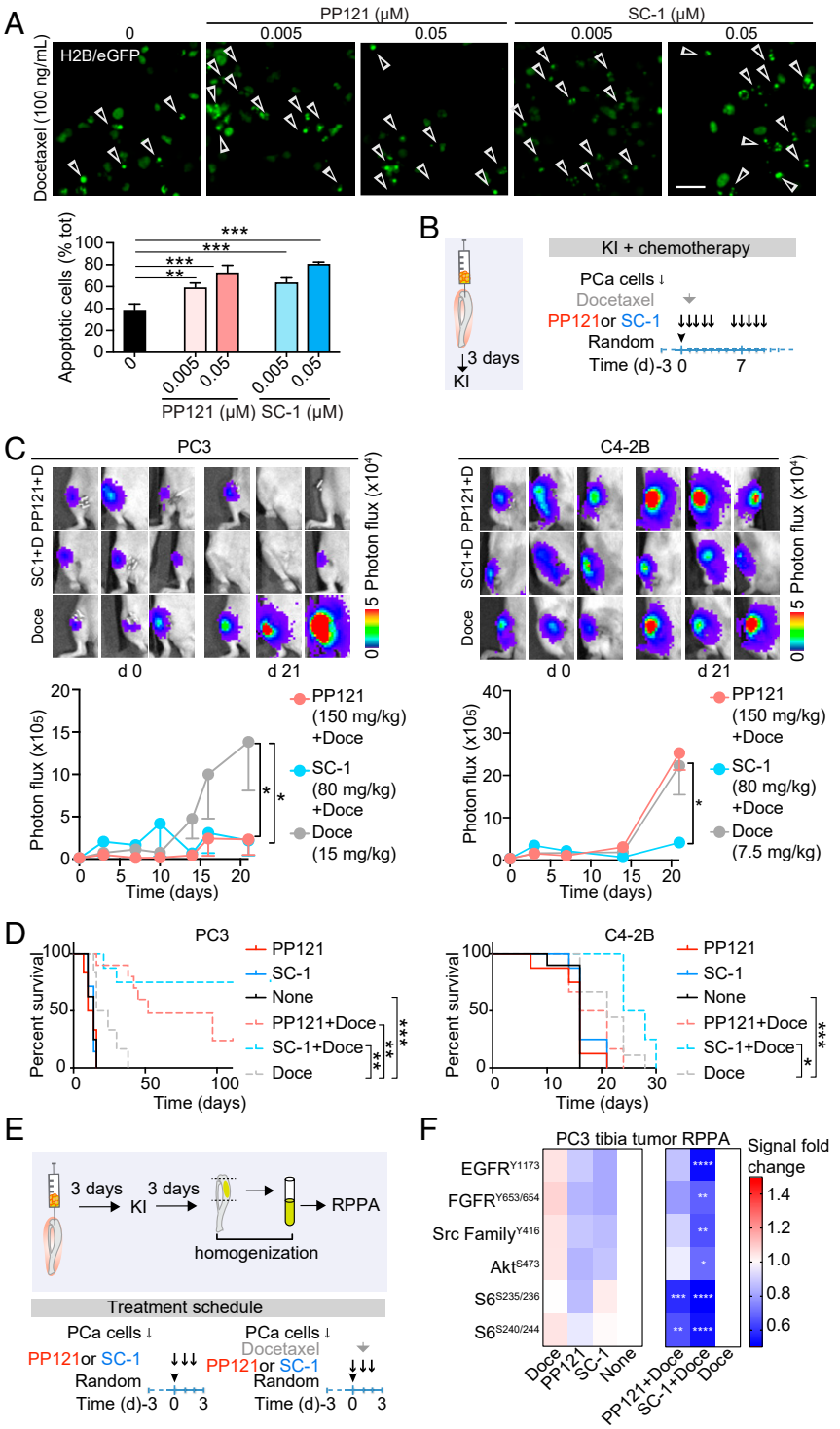


Fig. 5. Response to KI treatment by prostate cancer cells (PCa) cells in bone in combination with chemotherapy. (*A*) PC3 dual-color cells were treated with docetaxel (100 ng/mL) and KIs (0.05 μM and 0.005 μM), and images of H2B/eGFP nuclei were captured by the epifluorescence microscope. The number of apoptotic cells was quantified and reported as percent of the total number of cells present in each picture, one picture/well, three wells/treatment, and mean ± SD is shown. Arrowheads represent apoptosis. (Scale bar, 20 μm.) (*B*) Schematic representation of in vivo treatment schedule. PCa cells were implanted by intratibial injection, and the response to KI treatment was assessed longitudinally monitoring the bioluminescence signal. At day 3, after tumor implantation (2.5×10^5 PC3 cells/ tibia and 5×10^5 C4-2B cells/tibia), mice were randomized and treated with the indicated KI doses in combination with docetaxel. (*C*) KI treatment response of PC3 and C4-2B cells in bone. Representative bioluminescence images and tumor growth curves are shown, mean ± SD, and $n = 8$ to 10 tibiae per group. (*D*) Survival was estimated over time. $^*P < 0.05$, $^{**}P < 0.01$, $^{***}P < 0.001$, and one-way ANOVA followed by Tukey's honestly significant difference post hoc test. (*E*) Schematic representation of short-term in vivo treatment schedule and the subsequent analysis by RPPA. PC3 tumors implanted in mouse tibiae were allowed to grow for 3 d and then randomized and treated with KIs alone or in combination with docetaxel. After 3 d of treatment, tumors were surgically lysed, homogenized, and subjected to RPPA. (*F*) Heatmap of RPPA signal from short-term in vivo PC3 tibia xenografts treated with KI monotherapy or combination therapy with docetaxel. Signal is normalized to β-actin and presented relative to untreated control (*Left heatmap*) or docetaxel monotherapy (*Right heatmap*). $^*P < 0.05$, $^{**}P < 0.01$, $^{***}P < 0.001$, $^{****}P < 0.0001$, and two-way ANOVA with Holm–Sidak multiple comparisons test. Doce, docetaxel; tot, total.

Downloaded by guest on January 7, 2022

patients who are more likely to benefit from specific mono or combination therapies (31, 41). The current focus in the field of prostate cancer treatment has been on combining docetaxel with KIs, such as those targeting PI3K/mTOR (42), Aurora kinase A (37), mTOR (everolimus) (43), AKT (36, 44), and FAK (45). Our work suggests that the effectiveness of the treatment may be improved through the use of multitargeted KIs and that polypharmacology may play an important role in the context of CRPC in which multiple kinases seem to be involved. As a next step, we performed a principal component analysis on all of the FDA-approved KIs profiled in our dataset, alongside PP121 and SC-1 (*SI Appendix*, Fig. S9). Plotting the first two principal components (together accounting for 49.5% of the total variance) shows that ponatinib falls between PP121 and SC-1 and much closer to these tested compounds than any other FDA-approved agent. This indicates that the target profile of ponatinib is the most similar to that of PP121 or SC-1 and may therefore provide a promising opportunity for drug repurposing. Overall, the study bridges the gap between translational research and clinical results and paves the way for further investigations into the use of broadly multitargeted KIs in CRPC treatment.

Materials and Methods

Cell Culture. PC3, 22Rv1, and DU145 cells were purchased from the American Type Culture Collection. C4-2B cells were purchased from ViroMed laboratories. PC3, C4-2B, and 22Rv1 cells were cultured in Roswell Park Memorial Institute (RPMI) media supplemented with 10% fetal bovine serum (FBS), 1% penicillin/streptomycin, and 1% sodium pyruvate. DU145 cells were cultured in Dulbecco's Modified Eagle Medium (DMEM) supplemented with 10% FBS and 1% penicillin/streptomycin. Enzalutamide-resistant LNCaP42D cells (derived from LNCaP cells) were cultured in RPMI media supplemented with 10% FBS, 1% penicillin/streptomycin, and 10 μM enzalutamide. LuCaP35CR cells were cultured in DMEM supplemented with 10% FBS and 1% penicillin/streptomycin and 1× Glutamax. PC3 dual color (DC) cells expressing nuclear H2B/eGFP and cytoplasmic DsRed2 were from Anticancer; PC3 luciferase-expressing cells were a gift of Gary Gallick, The University of Texas (UT) MD Anderson Cancer Center, Houston, TX. Cells were cultivated in DMEM (Corning) supplemented with 10% FBS (Sigma-Aldrich) and penicillin–streptomycin (100 μg/mL each, Sigma-Aldrich). C4-2B cells (a gift of Timothy Thompson, UT MD Anderson Cancer Center) expressing luciferase were cultivated in RPMI (Corning) supplemented with 10% FBS (Sigma-Aldrich), penicillin–streptomycin (100μg/mL each, Sigma-Aldrich), and 1% Hepes. The identity of cancer cell lines was verified by the "Characterized Cell Line Core Facility," MD Anderson Cancer Center, through short tandem repeat DNA profiling. Adipose tissue-derived mesenchymal stem cells (hMSCs, ASC52telo telomerase reverse transcriptase immortalized from ATCC) were cultivated in MEM 1× (Corning) supplemented with 17% FBS (Sigma-Aldrich), penicillin–streptomycin (100 μg/mL each, Sigma-Aldrich), vitamins (Sigma-Aldrich), nonessential amino acids (Sigma-Aldrich), and sodium pyruvate (Gibco). To induce differentiation toward the osteoblastic lineage, hMSCs were kept in osteogenic induction medium (DMEM 1×, supplemented with 10% FBS, penicillin and streptomycin, 50 μg/mL ascorbic acid,10 mM β-glycerophosphate, and 0.1 μM dexamethasone from Sigma-Aldrich).

Drug Response and Quantification. Unless otherwise specified, all drug response data were collected by plating cells in 96-well tissue culture-treated plates, allowing cells to adhere overnight, and treated with small molecules suspended in DMSO. Drug dilutions were made using threefold serial dilutions in the appropriate media for each cell type, and each dose was administered to the cells in triplicate. Microscopy images were taken with an Incucyte using the 10× objective. Confluence as the percentage of total area covered by cells was quantified using the Incucyte ZOOM 2016B software.

Computational Analysis and Modeling. Unless otherwise specified, all dose–response plots, fitted curves, and interpolations were performed using GraphPad Prism version 7.03. Elastic net KiR models, predictions, and cross-validation plots were generated in R Studio version 1.0.153, running R version 3.4.1 "Single Candle," using custom scripts that employ the "glmnet" package (*SI Appendix, KiR Script*) (22), The input parameters to the cv.glmnet command were as follows: the residual kinase activities of the KIs in the training set as x-values, the Δconfluence of the corresponding KIs (as fraction of untreated control, ranging between 0 and 1) as y-values, no standardization of x-values, uniform observation weights and variable penalties, system-generated lambda sequence of 300 lambdas and a minimum ratio of 0.005, Gaussian (quantitative) family response type with naive algorithm, number of cross-validation folds equal to the number of observations (the length of the response vector; LOOCV), and alpha values ranging from 0.0 to 1.0, incrementing by 0.1 (the command is run iteratively for each value of alpha). Additional calculations and analyses were performed in Microsoft Excel 365. Heatmaps were generated either in R Studio using the "pheatmap" package (24) or in GraphPad Prism.

Reverse-Phase Protein Array. Protein microarrays were printed and processed, as described previously (21, 30). Briefly, PC3 or C4-2B cells were plated in 6-well plates at 500,000 cells/well and allowed to adhere overnight. The following morning, the cells were treated with PP121 or SC-1 at two doses (5 and 0.5 μM, plus DMSO control) for 1 h. Cells were then washed twice in phosphate-buffered saline (PBS), and cell lysates were prepared in 2% SDS lysis buffers, as described previously (46). Whole-cell lysates were printed onto 16-pad nitrocellulose-coated slides (Grace Biolabs, GBL505116) using Aushon 2470 microarrayer (Aushon BioSystems). Each sample was printed in triplicate and slides were stored at −20 °C until processing. RPPA slides were washed with 1 M Tris·HCl (pH 9.0) for 2 to 4 d to remove SDS. Slides were then washed 2 to 3 times with PBS for 5 min each and blocked with Odyssey blocking buffer (OBB) (Licor, 927–40000) for 1 h at room temperature. After blocking, arrays were incubated with primary antibodies in OBB at 4 °C overnight. The next day, arrays were washed thrice with PBS and incubated with IRDye-labeled secondary antibodies in OBB for 1 h at room temperature. Following incubation, slides were scanned using Licor Odyssey CLX Scanner (LiCOR). Total signal intensity from each spot was quantified using Array-Pro analyzer software package (Media Cybernetics). The measurement of a specific protein from an individual sample was normalized to total β-actin (Sigma-Aldrich, A1978).

In vivo samples had the following: tumors were surgically extracted from mice and kept cryopreserved until use. Small pieces of the tumors were homogenized and lysed in 2% SDS lysis buffer using a BioGen PRO200 homogenizer (PRO Scientific 01–01200). Samples were then processed, as described in the previous paragraph.

Polycaprolactone Scaffolds Fabrication. To fabricate scaffolds, polycaprolactone (43 kDa, Polysciences;Warrington, PA) was melted at 85 °C and printed at a collector velocity of 40 mm · s^{-1}, 5.0 kV, 1.0 bar, and at a distance of 10 mm using a 3DDiscovery Evolution printer, RegenHU, Switzerland. Scaffolds (6 mm in diameter) were designed using computer-aided design software BioCAD, according to the following characteristics: filament width of 35 μm, pore size of 40 μm, and scaffold height of 320 μm.

Generation of the BME. BMEs were generated, as previously described (44). In brief, hMSCs were seeded on the scaffolds (2.5×10^5 cells in 25 μL hMSC medium, 37 °C, 5% CO_2, and for 4 h) and then maintained in osteogenic medium for 30 d until complete differentiation. The osteogenic medium was refreshed weekly.

Generation of PC3 Spheroids. Spheroids of prostate cancer cells were generated through the hanging–drop method, as follows: 10^5 prostate cancer cells were incubated in standard cell culture medium supplemented with 20% methyl cellulose, 1% matrigel (BD Biosciences) and deposited as 25 μL drops on the lid of a 15-cm dish. The lid was inverted and the drops incubated overnight at 5% CO_2, 37 °C. After aggregation, spheroids were positioned in the center of the BME (overlaid with 75 μL of growth medium) in a 96-well plate using the bottom part of a 10-μL tip as a restrain that helps the positioning of the prostate cancer spheroids. BME cultures were incubated overnight at 37 °C, 5% CO, and moved to a 24-well plate with 1 mL prostate cancer cell culture medium.

Image Acquisition and Quantification of Prostate Cancer Growth. Images from 3D stacks were processed and analyzed through Fiji (47). Images of prostate cancer spheroids were acquired using an EVOS FL Cell Imaging System (AMG) equipped with 2× AMEP 4631 objective, numerical aperture = 0.06 or a confocal Leica MST66 microscope equipped with a Leica Z6 apochromatic zoom lens. Spheroid growth was quantified as fluorescent intensity, as the summation ($\sum$) of the gray value of all the pixels. The region of interest (ROI) was identified as the area occupied by each spheroid delimited with the magic wand tool. The background noise was determined as the mean gray value from a region outside the ROI (40 × 40 px) in a similar position for all images and used for background signal subtraction as follows: fluorescent intensity spheroids – (area spheroid × mean gray background). All images were acquired using the same setting at each time point.

Downloaded by guest on January 7, 2022

Treatment of PC3 on the BME. To address the effect of KIs on prostate cancer cells in 3D, spheroids made with PC3 dual-color cells (expressing nuclear H2B/eGFP and cytoplasmic DsRed2) were seeded on BMEs, treated at day 3 with KIs, and their growth followed through epifluorescence microscopy. The drugs were refreshed every 3 to 4 d.

Treatment of PC3 Dual-Color Cells in 2D as Monotherapy or Combination Therapy with Docetaxel. For dose–response studies, PC3 cells were seeded at a concentration of 1,000 cells/well and incubated overnight at 5% CO_2, 37 °C. The day after, KIs at different concentrations (5 μm to 0.005 μM, in quadruplicate) were added to the culture in complete medium. Cell growth was measured 1, 3, and 5 d posttreatment as follows: Cells were fixed for 30 min in ice-cold ethanol (200 μL/well), incubated for 30 min with crystal violet 0.25% in 20% methanol (40 μL/well), washed with water, and the signal detected using a plate reader at 570 optical density.

For studies on the cytotoxic activity of KIS, PC3DC were seeded at a concentration of 2,000 cells/well and incubated overnight at 5% CO_2, 37 °C. The day after, KIs were added to the culture at 5 μm to 0.005 μM, in quadruplicate. After 3 d, images were acquired at the EVOS microscope. Combination studies with docetaxel were carried out similarly. KIs were added to the culture at 0.05 or 0.005 μM (in quadruplicate), and docetaxel was added 1 d after KI treatment at 100 ng/mL After 3 d, images were acquired at the EVOS microscope.

Kinase Inhibitor Treatment In Vivo. Animal studies were approved by the Institutional Animal Care and Use Committee of The University of Texas MD Anderson Cancer Center and performed according to the institutional guidelines for animal care and handling. Athymic nude and nonobese diabetic–severe combined immunodeficiency (NOD-SCID) mice were injected with luciferase-expressing PC3 and C4-2B cells, respectively.

For subcutaneous tumors, mice were injected with 5×10^6 PC3 cells/mouse or 6×10^6 C4-2B cells/mouse subcutaneously, in 30% Matrigel in PBS ($n = 5$ to 8 mice/group). After 10 d, mice were randomized and treatment started. The growth of C4-2B tumors was monitored through macroscopic bioluminescence imaging using an IVIS 200 imaging system (PerkinElmer). The growth of PC3 tumors was monitored measuring tumor volume using a caliper.

For bone tumors, mice were injected with 2.5×10^5 PC3 cells/mouse or 1×10^6 C4-2B cells/mouse intratibial (8 to 10 tibiae/group) in PBS, randomized after 3 d, and treatment started. The growth of tumors was monitored through macroscopic bioluminescence imaging using an IVIS 200 imaging system. In survival studies, photon flux values of 1.2×10^6 or 2×10^6 (total counts) were considered as the end point for PC3- or C4-2B–implanted mice, respectively.

For in vivo treatments, mice received KI treatment 5 d/wk for 2 wk. Mice were administered a total daily dose of 150 mg/kg PP121 (Tocris) in 10% DMSO (Sigma-Aldrich), 40% polyethylene glycol (PEG)-300 (Sigma-Aldrich), 5% TWEEN-80 (Sigma-Aldrich), and 45% PBS through oral gavage (100 μl volume/administration, 75 mg/kg twice a day) or 80 mg/kg of SC-1 (Selleckchem) in 10% 2methyl2pirrolidinone (Sigma-Aldrich) and 90% PEG-300 (Sigma-Aldrich) through oral gavage (100 μL volume/administration, 40 mg/kg twice a day). For combination therapy, athymic nude mice were administered 15 mg/kg docetaxel (Sanofi) by intraperitoneal injection, while NOD-SCID mice were given 7.5 mg/kg docetaxel at day 5 after cell injection.

Quantification and Statistical Analysis. Statistical analysis was performed using GraphPad Prism 7.0 (GraphPad Software). To address the difference among different groups, one-way ANOVA was performed followed by Tukey's honestly significant difference post hoc test. All statistical tests were two sided, and a P value of less than 0.05 was considered statistically significant. Statistical analysis of RPPA data were done in GraphPad Prism version 7.03 using a two-way ANOVA with a Holm–Sidak multiple comparisons test.

Data Availability. All study data are included in the article and/or supporting information.

ACKNOWLEDGMENTS. This work was supported by the NIH/National Cancer Institute (NCI) (Grants K22CA201229, P30CA015704, 3 U24 CA209923-01S1, and P50CA097186). T.B. is a recipient of the Fred Hutch Interdisciplinary Training Grant Dual Mentor Fellowship in Cancer Research (T32CA080416). T.S.G. is supported in part by the NSF under Grant No. 2047289, Research Scholar Grant 133870-RSG-19-197-01-CDD from the American Cancer Society, the Translational Adult Glioma Award from The Ben and Catherine Ivy Foundation, and a Conquer Cancer Now Award from The Concern Foundation. P.S.N. is supported by the Pacific Northwest Prostate Cancer Specialized Program of Research Excellence (SPORE) CA097186 and Congressionally Directed Medical Research Programs Award W81XWH-18-1-0347. E.D. is supported by the American Association for Cancer Research-Bayer Innovation and Discovery Grant and the MD Anderson Cancer Center Prostate Cancer SPORE (P50 CA140388-09). The Genitourinary Cancers Program of the Cancer Center Support Grant shared resources at MD Anderson Cancer Center and is supported by NIH/NCI Award P30 CA016672. The Center for Engineering Complex Tissue is supported by the NIH (Grant P41 EB023833). We thank Dr. Eva Corey and Dr. Nora Navone for providing PDX samples for ex vivo assays. We thank Dr. Milka Kostic, Dr. Andrew Hsieh, and Dr. Paul Corn for helpful comments on the manuscript.

1. H. Sung *et al*., Global cancer statistics 2020: GLOBOCAN estimates of incidence and mortality worldwide for 36 cancers in 185 countries. *CA Cancer J. Clin.* **71**, 209–249 (2021).
2. R. L. Siegel, K. D. Miller, A. Jemal, Cancer statistics, 2019. *CA Cancer J. Clin.* **69**, 7–34 (2019).
3. G. Gandaglia *et al*., Distribution of metastatic sites in patients with prostate cancer: A population-based analysis. *Prostate* **74**, 210–216 (2014).
4. E. G. Bluemn *et al*., Androgen receptor pathway-independent prostate cancer is sustained through FGF signaling. *Cancer Cell* **32**, 474–489.e6 (2017).
5. J. M. Drake *et al*., Metastatic castration-resistant prostate cancer reveals intrapatient similarity and interpatient heterogeneity of therapeutic kinase targets. *Proc. Natl. Acad. Sci. U.S.A.* **110**, E4762–E4769 (2013).
6. J. M. Drake *et al*., Phosphoproteome integration reveals patient-specific networks in prostate cancer. *Cell* **166**, 1041–1054 (2016).
7. F. Ardito, M. Giuliani, D. Perrone, G. Troiano, L. Lo Muzio, The crucial role of protein phosphorylation in cell signaling and its use as targeted therapy (review). *Int. J. Mol. Med.* **40**, 271–280 (2017).
8. S. Knapp, New opportunities for kinase drug repurposing and target discovery. *Br. J. Cancer* **118**, 936–937 (2018).
9. P. Wu, T. E. Nielsen, M. H. Clausen, FDA-approved small-molecule kinase inhibitors. *Trends Pharmacol. Sci.* **36**, 422–439 (2015).
10. S. Klaeger *et al*., The target landscape of clinical kinase drugs. *Science* **358**, eaan4368 (2017).
11. T. Anastassiadis, S. W. Deacon, K. Devarajan, H. Ma, J. R. Peterson, Comprehensive assay of kinase catalytic activity reveals features of kinase inhibitor selectivity. *Nat. Biotechnol.* **29**, 1039–1045 (2011).
12. A. Lin *et al*., Off-target toxicity is a common mechanism of action of cancer drugs undergoing clinical trials. *Sci. Transl. Med.* **11**, eaaw8412 (2019).
13. M. A. Ojemuyiwa, R. A. Madan, W. L. Dahut, Tyrosine kinase inhibitors in the treatment of prostate cancer: Taking the next step in clinical development. *Expert Opin. Emerg. Drugs* **19**, 459–470 (2014).
14. T. S. Gujral, L. Peshkin, M. W. Kirschner, Exploiting polypharmacology for drug target deconvolution. *Proc. Natl. Acad. Sci. U.S.A.* **111**, 5048–5053 (2014).
15. M. Levis, Midostaurin approved for FLT3-mutated AML. *Blood* **129**, 3403–3406 (2017).
16. T. S. Gujral *et al*., A noncanonical Frizzled2 pathway regulates epithelial-mesenchymal transition and metastasis. *Cell* **159**, 844–856 (2014).
17. N. Arang *et al*., Identifying host regulators and inhibitors of liver stage malaria infection using kinase activity profiles. *Nat. Commun.* **8**, 1232 (2017).
18. S. Rata *et al*., An optimal set of inhibitors for reverse engineering via kinase regularization. bioRxiv [Preprint] (2020). https://www.biorxiv.org/content/10.1101/2020.09.26.312348v1. Accessed 30 September 2020.
19. D. Cunningham, Z. You, In vitro and in vivo model systems used in prostate cancer research. *J. Biol. Methods* **2**, e17 (2015).
20. H. Zou, T. Hastie, Regularization and variable selection via the elastic net. *J. R. Stat. Soc. B* **67**, 301–320 (2005).
21. T. S. Gujral, M. W. Kirschner, Hippo pathway mediates resistance to cytotoxic drugs. *Proc. Natl. Acad. Sci. U.S.A.* **114**, E3729–E3738 (2017).
22. J. Friedman, T. Hastie, R. Tibshirani, Regularization paths for generalized linear models via coordinate descent. *J. Stat. Softw.* **33**, 1–22 (2010).
23. M. Krzywinski, N. Altman, Multiple linear regression. *Nat. Methods* **12**, 1103–1104 (2015).
24. T. Bello, T. S. Gujral, KInhibition: A kinase inhibitor selection portal. *iScience* **8**, 49–53 (2018).
25. J. C. Araujo *et al*., Docetaxel and dasatinib or placebo in men with metastatic castration-resistant prostate cancer (READY): A randomised, double-blind phase 3 trial. *Lancet Oncol.* **14**, 1307–1316 (2013).
26. R. Sivakumar *et al*., Organotypic tumor slice cultures provide a versatile platform for immuno-oncology and drug discovery. *Oncoimmunology* **8**, e1670019 (2019).
27. B. Apsel *et al*., Targeted polypharmacology: Discovery of dual inhibitors of tyrosine and phosphoinositide kinases. *Nat. Chem. Biol.* **4**, 691–699 (2008).
28. H.-Y. Che, H.-Y. Guo, X.-W. Si, Q.-Y. You, W.-Y. Lou, PP121, a dual inhibitor of tyrosine and phosphoinositide kinases, inhibits anaplastic thyroid carcinoma cell proliferation and migration. *Tumour Biol.* **35**, 8659–8664 (2014).
29. S. Chen *et al*., Self-renewal of embryonic stem cells by a small molecule. *Proc. Natl. Acad. Sci. U.S.A.* **103**, 17266–17271 (2006).
30. T. S. Gujral *et al*., Profiling phospho-signaling networks in breast cancer using reverse-phase protein arrays. *Oncogene* **32**, 3470–3476 (2013).

Downloaded by guest on January 7, 2022

31. S. I. Park *et al*., Targeting SRC family kinases inhibits growth and lymph node metastases of prostate cancer in an orthotopic nude mouse model. *Cancer Res.* **68**, 3323–3333 (2008).
32. J. M. Drake *et al*., Oncogene-specific activation of tyrosine kinase networks during prostate cancer progression. *Proc. Natl. Acad. Sci. U.S.A.* **109**, 1643–1648 (2012).
33. A. Goc *et al*., PI3 kinase integrates Akt and MAP kinase signaling pathways in the regulation of prostate cancer. *Int. J. Oncol.* **38**, 267–277 (2011).
34. H. Zheng *et al*., Therapeutic antibody targeting tumor-and osteoblastic niche-derived jagged1 sensitizes bone metastasis to chemotherapy. *Cancer Cell* **32**, 731–747.e6 (2017).
35. Y.-C. Lee *et al*., Identification of bone-derived factors conferring de novo therapeutic resistance in metastatic prostate cancer. *Cancer Res.* **75**, 4949–4959 (2015).
36. S. J. Crabb *et al*., ProCAID: A phase I clinical trial to combine the AKT inhibitor AZD5363 with docetaxel and prednisolone chemotherapy for metastatic castration resistant prostate cancer. *Invest. New Drugs* **35**, 599–607 (2017).
37. J. N. Graff *et al*., Open-label, multicenter, phase 1 study of alisertib (MLN8237), an aurora A kinase inhibitor, with docetaxel in patients with solid tumors. *Cancer* **122**, 2524–2533 (2016).
38. K. Fizazi *et al*.; LATITUDE Investigators, Abiraterone plus prednisone in metastatic, castration-sensitive prostate cancer. *N. Engl. J. Med.* **377**, 352–360 (2017).
39. I. D. Davis *et al*.; ENZAMET Trial Investigators and the Australian and New Zealand Urogenital and Prostate Cancer Trials Group, Enzalutamide with standard first-line therapy in metastatic prostate cancer. *N. Engl. J. Med.* **381**, 121–131 (2019).
40. W. K. Oh *et al*., Real-world outcomes in patients with metastatic castration-resistant prostate cancer receiving second-line chemotherapy versus an alternative androgen receptor-targeted agent (ARTA) following early progression on a first-line ARTA in a US community oncology setting. *Urol. Oncol.* **36**, 500.e1–500.e9 (2018).
41. J. C. Araujo *et al*., Dasatinib combined with docetaxel for castration-resistant prostate cancer: Results from a phase 1-2 study. *Cancer* **118**, 63–71 (2012).
42. Y. Yasumizu *et al*., Dual PI3K/mTOR inhibitor NVP-BEZ235 sensitizes docetaxel in castration resistant prostate cancer. *J. Urol.* **191**, 227–234 (2014).
43. H. Alshaker *et al*., Combination of RAD001 (everolimus) and docetaxel reduces prostate and breast cancer cell VEGF production and tumour vascularisation independently of sphingosine-kinase-1. *Sci. Rep.* **7**, 3493 (2017).
44. C. Paindelli, N. Navone, C. J. Logothetis, P. Friedl, E. Dondossola, Engineered bone for probing organotypic growth and therapy response of prostate cancer tumoroids in vitro. *Biomaterials* **197**, 296–304 (2019).
45. H.-M. Lin *et al*., Effect of FAK inhibitor VS-6063 (defactinib) on docetaxel efficacy in prostate cancer. *Prostate* **78**, 308–317 (2018).
46. K. Luckert *et al*., A dual array-based approach to assess the abundance and post-translational modification state of signaling proteins. *Sci. Signal.* **5**, pl1 (2012). Correction in: *Sci. Signal.* **5**, er5 (2012).
47. J. Schindelin *et al*., Fiji: An open-source platform for biological-image analysis. *Nat. Methods* **9**, 676–682 (2012).

Downloaded by guest on January 7, 2022